Available online at www.sciencedirect.com
SCIENCE DIRECT®
ELSEVIER
International Journal of Solids and Structures 42 (2005) 3807–3832
INTERNATIONAL JOURNAL OF SOLIDS and STRUCTURES
www.elsevier.com/locate/ijsolstr

Universal scaling functions for continuous stiffness nanoindentation with sharp indenters

Lugen Wang, S.I. Rokhlin *

Laboratory for Multiscale Materials Processing and Characterization, Edison Joining Technology Center, The Ohio State University, 1248 Arthur E. Adams Drive, Columbus, OH 43221, USA

Received 5 August 2004; received in revised form 11 November 2004
Available online 19 December 2004

Abstract

This paper presents numerical and scaling analysis for continuous stiffness measurement (CSM) in nanoindentation tests. It shows numerically and experimentally that in CSM with sharp indenters the indentation displacement is proportional to stiffness and load is proportional to stiffness squared. The slopes of the two linear functions have been represented by two universal scaling functions obtained using self-similarity analysis. The scaled functions depend only on two governing parameters for materials with power law strain hardening behavior. One is the strain hardening exponent and the other is the nondimensional parameter $\tilde{\varepsilon}_Y^* = \sigma_Y \tan\theta/E^*$ where $E^* = E/(1-\nu^2)$, E is Young's modulus, σ_Y is yield stress, ν is Poisson's ratio and θ is the equivalent half angle of the sharp indenter. The large deformation finite element method (FEM) has been used to simulate CSM nanoindentation and validate the universality of the functions over scaling parameters. To simulate small displacement oscillations applied on the indenter during CSM nanoindentation linear perturbation in the FEM computation has been used. Explicit equations for the universal scaling functions with and without friction have been obtained by fitting numerical results. The scaling functions asymptotically approach the elastic solution at low plasticity ($\tilde{\varepsilon}_Y^* \to \infty$) and the full plastic solution at high plasticity ($\tilde{\varepsilon}_Y^* \to 0$) and are valid in the elasto-plastic regime. Applicability of the scaling functions for nonpower-law stress–strain relations has been demonstrated with use of two representative strains.

Keywords: Indentation; Scaling; Finite element; Elasto-plastic

* Corresponding author. Tel.: +1 614 292 7823; fax: +1 614 292 3395.
E-mail addresses: wang.422@osu.edu (L. Wang), rokhlin.2@osu.edu (S.I. Rokhlin).

0020-7683/$ - see front matter © 2004 Elsevier Ltd. All rights reserved.
doi:10.1016/j.ijsolstr.2004.11.012

1. Introduction

Instrumented micro and nanoindentation is becoming an increasingly important method of measuring elasto-plastic properties on small samples (Doerner and Nix, 1986; Oliver and Pharr, 1992, 2004; Tabor, 1996; Fischer-Cripps, 2002; Li and Bhushan, 2002). With very small diamond indenter tips and high resolution of force and displacement sensing in nanoindentation instruments, the measurements are performed at the nano/micro scale. The material properties are determined from analysis of displacement/load behavior during loading and unloading cycles (for a review of different methods see Fischer-Cripps, 2002). The relation between displacement and load during loading and unloading has been comprehensively studied using finite element simulations (Larsson et al., 1996; Bhattacharya and Nix, 1988; Cheng and Cheng, 1998; Bolshakov and Pharr, 1998; Knapp et al., 1999; Dao et al., 2001; Sakai et al., 2004). To reduce the number of governing parameters and formulate general relations between load and indentation depth and the initial slope in unloading (Fig. 1), dimensional analysis has been applied to obtain scaling relations for conical indentation in elasto-plastic solids (Cheng and Cheng, 1998, 1999, 2000; Dao et al., 2001).

Traditionally, the Young's modulus and the indentation hardness (Doerner and Nix, 1986; Oliver and Pharr, 1992) are determined from analysis of the indentation loading and unloading responses based on Sneddon's elastic solution (Sneddon, 1965). This method allows one to determine the reduced Young's modulus and hardness with different precision which is sometimes difficult to evaluate due to plasticity-induced piling-up. There is significant interest in determining elasto-plastic material properties (Young's modulus E, yield stress σ_Y and strain hardening exponent n) from nanoindentation tests as has been done from uniaxial tensile/compression experiments. Different investigators approach this task utilizing an inversion of the finite element model (FEM) by fitting the loading and unloading force–displacement nanoindentation response (Bhattacharya and Nix, 1988; Suresh and Giannakopoulos, 1998; Knapp et al., 1999; Giannakopoulos and Suresh, 1999; Constantinescu and Tardieu, 2001; Tunvisut et al., 2001; Xu and Rowcliffe, 2002; Mata and Alcalá, 2003). However, direct inversion of FEM computations is very expensive computationally. In this regard significant progress has been achieved by Dao et al. (2001), who have developed, based on extensive FEM simulation, fitting functions for a wide range of properties for materials with power-law strain hardening behavior. Using these functions the inversion process to determine the elasto-plastic material properties from instrumented indentation tests is significantly simplified. However it was understood that only two elasto-plastic parameters could be found from one indentation loading and

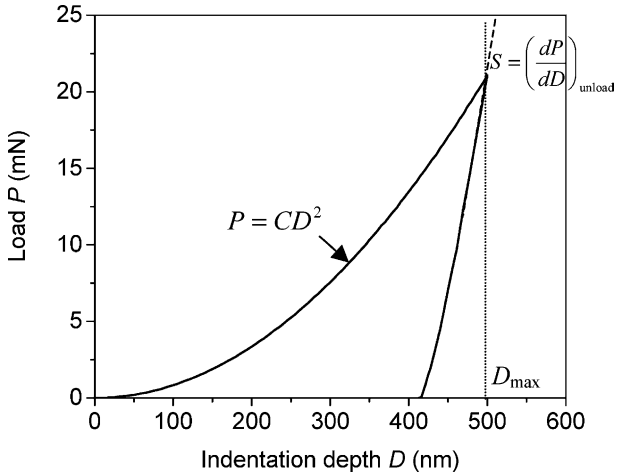

Fig. 1. A typical indentation load–depth relation of an elasto-plastic semispace material for a conical or Berkovich indenter.

unloading response (Cheng and Cheng, 1999; Chollacoop et al., 2003; Bucaille et al., 2003). To determine all three parameters for materials with power law strain hardening (E, σ_Y and n), it was proposed to use indentation results obtained with two sharp indenters with different apex angles (Chollacoop et al., 2003; Bucaille et al., 2003).

An alternative method of nanoindentation testing is the continuous stiffness measurement (CSM) technique (Oliver and Pharr, 1992; Li and Bhushan, 2002). In this technique, the stiffness is measured continuously during the indentation test by imposing a small oscillating force during loading. This is particularly important for testing of material systems that have elastic properties varying with depth, for example thin film systems.

In this paper, we study the relations between load, displacement and dynamic stiffness in CSM nanoindentation of homogeneous materials using finite element simulation and scaling analysis. Based on these we obtain explicit universal scaling relations. Our scaling analysis is based on the small deformation formalism. It shows that for a power-law strain hardening stress–strain relation the scaling functions depend on only two parameters: the power law exponent n and a parameter $\tilde{\varepsilon}_Y^* = \sigma_Y \tan\theta/E^*$ introduced originally by Johnson (1970) and used by others (Storåkers et al., 1997; Mesarovic and Fleck, 1999; Larsson, 2001). It will be of great interest to extend this conclusion theoretically to large deformation theory. However this is beyond the scope of this paper and the applicability of the scaling functions obtained to the large deformation formulation necessary for description of indentation with sharp indenters is validated numerically. We also show how our results can be extended to materials with more general than the power-law strain hardening stress–strain relation. Our scaling approach is different from previous studies (Cheng and Cheng, 1998, 2000; Dao et al., 2001) in that the scaling includes the conical apex angle and our universal fitting functions of the numerical results are based on asymptotic behavior of the elastic–plastic solution in the elastic and full plastic regimes.

2. Background and problem statement

Fig. 1 shows a typical indentation response for sharp indenters such as conical and Berkovich indenters. From the dimensional and similarity analysis (Cheng and Cheng, 1998, 2000; Dao et al., 2001), the loading response for such indenters is governed by the parabolic force–displacement relation

$$P = CD^2, \tag{1}$$

where P is the indentation force and D is the indentation depth. The unloading response is a nearly elastic recovery, which is characterized by the initial unloading slope S (unloading stiffness). Therefore from the loading–unloading nanoindentation test with a sharp indenter, one may determine two independent parameters: the curvature of the loading response C [N/m^2] and the initial unloading slope S at maximum indentation depth $D_{\max}$ (Fig. 1).

It has been demonstrated in several studies that elasto-plastic properties of materials may be determined from the instrumental loading–unloading cycle using finite element simulations and optimizing fitting of the indentation response by a model (for comprehensive review see Dao et al., 2001). However such an approach is computationally expensive since such an analysis must be performed for each separate experimental case. The approach may be significantly facilitated by introducing universal scaling functions using dimensional analysis which relate indentation parameters S and C to elasto-plastic material properties and indenter geometry. In this analysis, the stress σ–strain ε relation under uniaxial test is assumed to be given by

$$\sigma = \begin{cases} E\varepsilon, & \varepsilon < \varepsilon_Y, \\ R\varepsilon^n, & \varepsilon \geqslant \varepsilon_Y, \end{cases} \tag{2}$$

where E is Young's modulus, $\varepsilon_Y = \sigma_Y/E$ the strain at yield stress σ_Y, n the strain hardening exponent and R a strength coefficient. To assure continuity of stress–strain curve at yielding $\sigma_Y = E\varepsilon_Y = R\varepsilon_Y^n$, the strength coefficient R is related to yield stress and strain as $R = \sigma_Y/\varepsilon_Y^n$. More general stress–strain relations will be addressed in Section 8.

To reduce the number of variables affecting nanoindentation with sharp indenters, Cheng and Cheng (1998), and Dao et al. (2001) have proposed scaling functions for the coefficient C in (1) and unloading slope S in the form

$$C = \sigma_r \Pi_{1\theta}\left(\frac{E^*}{\sigma_r}, \theta\right), \tag{3a}$$

$$S = E^* D_{max} \Pi_{2\theta}\left(\frac{E^*}{\sigma_r}, n, \theta\right). \tag{3b}$$

where $E^* = E/(1-\nu^2)$ is the reduced modulus (ν is Poisson's ratio), σ_r is the representative stress and θ is the half apex angle of the conical indenter. The scaling function $\Pi_{1\theta}$ is independent of the strain hardening exponent n if an appropriate representative strain ε_r is selected (Dao et al., 2001). The empirical expressions for functions $\Pi_{1\theta}$ and $\Pi_{2\theta}$ have been found (Dao et al., 2001) by fitting the numerical results obtained with larger deformation finite element analysis (FEM). Bucaille et al. (2003) also showed that the parameter $C/\tan^2\theta$ is approximately independent of apex angle θ.

One of the modalities of nanoindentation testing is the continuous stiffness measurement (CSM) technique. In the CSM method the load P, displacement D and dynamic contact stiffness s, which equals the initial unloading slope S under quasi-static approximation, are measured continuously during loading. Therefore in this mode of operation, besides the P–D relation (1), one also obtains P–s and D–s relations during loading. Fig. 2 presents experimental CSM data (open circles) obtained by an MTS Nanoindenter® XP instrument using a standard Berkovich tip on an Al2024 T3 sample. The P–D^2 relation is shown in Fig. 2(a), the D–s in (b) and the P–s^2 in (c); the solid lines show linear fittings. As can be seen, for bulk homogeneous materials the indentation displacement D is linearly related to the dynamic stiffness s and the load P is linearly related to the square of s. From the loading response in the CSM measurement, we have

$$P = CD^2, \quad D = C_d s, \quad P = C_p s^2, \tag{4}$$

where C [N/m^2], C_d [m^2/N] and C_p [m^2/N] are the slopes of the linear functions obtained by fitting of the experimental data as shown in Fig. 2. The utility for nanoindentation of the $P \propto s^2$ relation has been discussed by Joslin and Oliver (1990). The parameters C_p, C_d and C depend on material elasto-plastic properties and tip geometry. From Eq. (4), one finds the relation $C = C_p/C_d^2$; thus there are only two independent parameters.

The relations (4) hold in general for indentation of homogeneous semispaces with Berkovich and other conical-equivalent indenters. Thus two independent parameters C_d and C_p can fully characterize the CSM indentation response with a sharp indenter. Below, using scaling analysis and large deformation finite element computations, we will investigate the relations of C_d and C_p to the elasto-plastic material properties and the indenter geometry. We will obtain nondimensional universal functions for these relations, using which one can simplify the inverse determination of the elasto-plastic properties from the CSM indentation measurements.

3. Scaling analysis

Analytical solutions for conical indentation are limited to elastic (Sneddon, 1965) and rigid-plastic solids (Lockett, 1963). For general elasto-plastic solids, numerical methods have been extensively used. However,

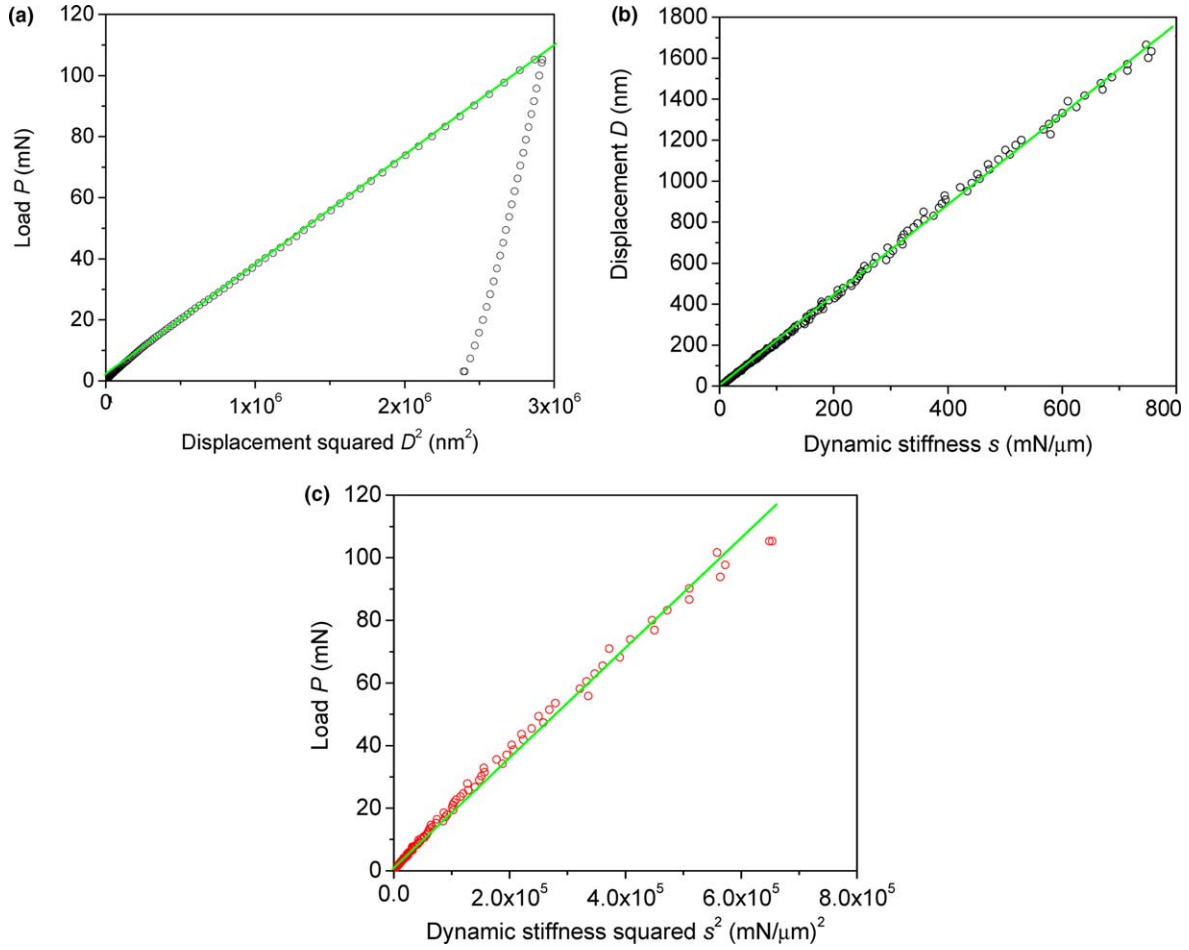

Fig. 2. Typical CSM nanoindentation responses for Al2024 T3. (a) Relation between displacement square and load. (b) Relation between displacement and dynamic stiffness s. (c) relation between load and square of dynamic stiffness s^2.

because there are five governing variables (apex angle θ and four material properties E, v, n, σ_Y), it is difficult to obtain numerically general relations between them and the experimental parameters (C, C_d, C_p). However, due to the geometrical similarity of the conical indenter, it is possible to obtain general dependences of the experimental parameters (C, C_d, C_p) with the five governing parameters (θ, E, v, n, σ_Y) thus reducing the number of free variables.

For spherical indentation, Hill et al. (1989) developed a self-similar solution for a power law nonlinear elastic material and gave a theoretical interpretation of Meyer's law in the Brinell hardness test. Storåkers et al. (1997) applied similar analysis to more general constitutive properties of materials and tip geometry. In this section following Hill et al. (1989), we will use the concept of self-similarity analysis to obtain scaling formulations for the two independent experimentally-measurable parameters C_d and C_p. To do this we will deal with the small deformation elasto-plastic formulation which in the following section will be validated and quantified by FEM computations within the large deformation formalism.

The sharp indenters such as Berkovich are approximated by conical indenters with equivalent half angles. A schematic of the conical indentation is given in Fig. 3 where cases for piling-up (Fig. 3a) and

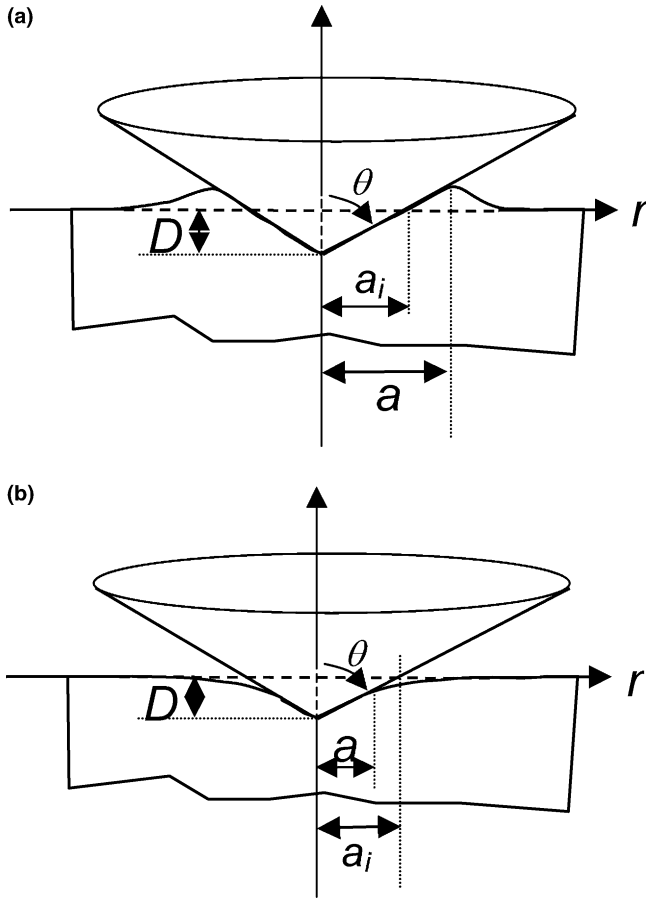

Fig. 3. Schematic of the conical indentation. (a) Material piling-up, $a_i < a$ and (b) sinking-in, $a_i > a$.

sinking-in (Fig. 3b) are shown. Within a small strain formulation, the constitutive equation of the homogeneous substrate is given by Hooke's law in the elastic regime. In the elasto-plastic regime, the von Mises yield criterion and the associated Prandtl–Reuss flow rule are used (Mendelson, 1968; Larsson et al., 1996):

$$\dot{\sigma}_{ij} = \frac{E}{1+v}\left\{\delta_{ik}\delta_{il} + \frac{v}{1-2v}\delta_{ij}\delta_{kl} - \frac{E}{1+v}\frac{3\sigma'_{ij}\sigma'_{kl}}{2\sigma_e^2\left(\frac{2}{3}B + \frac{E}{1+v}\right)}\right\}\dot{\varepsilon}_{ij}, \tag{5}$$

where σ_{ij} is the Cauchy stress; E is Young's modulus, v is Poisson's ratio, δ_{il} is Kronecker's identity tensor, ε_{ij} is the strain tensor and $\sigma'_{ij} = \sigma_{ij} - \sigma_{kk}\delta_{ij}/3$ is the deviatoric stress. $\sigma_e = \left(\frac{3}{2}\sigma'_{ij}\sigma'_{ij}\right)^{1/2}$ is the von Mises effective stress. The dot superscript represents small increments. $B = \mathrm{d}\sigma/\mathrm{d}\varepsilon_p$ is the slope of the stress–plastic strain (σ–ε_p) relation obtained by uniaxial test. The stress–strain relation under uniaxial test is assumed to be given by Eq. (2).

The boundary conditions for conical indentations, as shown schematically in Fig. 3, are

$$\sigma_{rz} = \sigma_{zz} = 0 \quad \text{for } r > a \tag{6a}$$

and

$$\sigma_{rz} = 0, \quad u_z = D - r/\tan\theta \quad \text{for } r \leqslant a, \tag{6b}$$

where θ is the half angle of the conical indenter and we assume no friction between contact surfaces. The constitutive Eqs. (2), (5) and the boundary conditions (6) together with the equilibrium equation

$$\sigma_{ij,i} = 0, \tag{7}$$

define uniquely an indentation solution.

From Eqs. (5)–(7) follows that the solutions (contact stress, indentation displacement D) are functions of five governing parameters E, v, σ_Y, n, θ. To reduce the number of variables, we introduce scaled spatial variables $\tilde{x}_i$, $\tilde{r}$ and displacement $\tilde{u}_i$ as

$$\tilde{x}_i = x_i/a, \quad \tilde{r} = r/a, \quad \tilde{u}_i = u_i \tan\theta/a. \tag{8}$$

The normalized strain $\tilde{\varepsilon}_{ij}$ and stress $\tilde{\sigma}_{ij}$ are given by

$$\tilde{\varepsilon}_{ij} = \varepsilon_{ij}\tan\theta, \quad \tilde{\sigma}_{ij} = \sigma_{ij}/\sigma_Y. \tag{9}$$

We also define a nondimensional parameter $\tilde{\varepsilon}_Y = \varepsilon_Y \tan\theta$ and reduced parameter

$$\tilde{\varepsilon}^*_Y = \frac{\sigma_Y \tan\theta}{E^*}, \tag{10}$$

where $E^* = E/(1-v^2)$. The universal parameter $\tilde{\varepsilon}^*_Y$ is the normalized yield strain. From Eq. (9), for the normalized stress–strain slope $\widetilde{B}$ we have $\widetilde{B} = \mathrm{d}\tilde{\sigma}/\mathrm{d}\tilde{\varepsilon}_p = B/\tilde{\varepsilon}_Y$. The parameter $\tilde{\varepsilon}^*_Y$ and its inverse $1/\tilde{\varepsilon}^*_Y = E^*/(\sigma_Y \tan\theta)$ have been introduced as governing parameters by Johnson (1970, 1985) for scaling and comparing of hardness data. They have been also used by a number of other researchers (Storåkers et al., 1997; Mesarovic and Fleck, 1999; Larsson, 2001; Sakai et al., 2004).

With the scaled variables defined by (8), (9), the indentation problem is reformulated as: the Prandtl–Reuss equations

$$\dot{\tilde{\sigma}}_{ij} = \frac{1}{(1+v)\tilde{\varepsilon}_Y}\left\{\delta_{ik}\delta_{il} + \frac{v}{1-2v}\delta_{ij}\delta_{kl} - \frac{1}{1+v}\frac{3\tilde{\sigma}'_{ij}\tilde{\sigma}'_{kl}}{2\tilde{\sigma}_e^2\left(\frac{2}{3\lambda}\widetilde{B} + \frac{1}{1+v}\right)}\right\}\dot{\tilde{\varepsilon}}_{ij}, \tag{11}$$

the stress–strain relation

$$\tilde{\sigma} = \begin{cases} \tilde{\varepsilon}/\tilde{\varepsilon}_Y, & \tilde{\varepsilon} < \tilde{\varepsilon}_Y, \\ (\tilde{\varepsilon}/\tilde{\varepsilon}_Y)^n, & \tilde{\varepsilon} \geqslant \tilde{\varepsilon}_Y \end{cases} \tag{12}$$

and boundary conditions

$$\tilde{\sigma}_{rz} = \tilde{\sigma}_{zz} = 0 \quad \text{for } \tilde{r} > 1, \tag{13a}$$

and

$$\tilde{\sigma}_{rz} = 0, \quad \tilde{u}_z = \frac{D\tan\theta}{a} - \tilde{r} \quad \text{for } \tilde{r} \leqslant 1. \tag{13b}$$

The scaled equilibrium equation is the same as Eq. (7) with the stresses σ_{ij} replaced by scaled stresses $\tilde{\sigma}_{ij}$.

With the scaled variables, the original indentation problem (5)–(7) is reduced to the scaled indentation problem (11)–(13). It follows from Eq. (11)–(13) that the original contact problem is mapped onto a unit circle in the scaled variables. One can see from Fig. 3 that the parameter $\frac{D\tan\theta}{a} = a_i/a$ is the ratio of nominal radius a_i to contact radius a and $\frac{D\tan\theta}{a}$ is an *invariant* of the contact problem. The parameters $\tilde{\varepsilon}_Y$, n and v are uniquely related to the invariant $\frac{D\tan\theta}{a}$ by Eq. (11)–(13). The Poisson's ratio may be included in the reduced modulus $E^* = E/(1-v^2)$ (Johnson, 1985) (this will be verified in Section 5); thus the two variables $\tilde{\varepsilon}_Y$, v may

be combined into one reduced variable $\tilde{\varepsilon}_Y^* = \tilde{\varepsilon}_Y/(1-\nu^2)$ (Eq. (10)). Therefore we can write $\frac{D\tan\theta}{a}$ as a function of $\tilde{\varepsilon}_Y^*$ and n only:

$$\frac{D\tan\theta}{a} = F_d(n, \tilde{\varepsilon}_Y^*). \tag{14}$$

Using the scaled variables, the indentation load P is given by

$$P = 2\pi \int_0^a \sigma_{zz} r \, dr = \pi a^2 \sigma_Y \int_0^1 \tilde{\sigma}_{zz} \, d\tilde{r}^2. \tag{15}$$

The load P is represented as a nondimensional parameter $\frac{P}{0.5\pi a^2 \sigma_Y}$ and is a function of $\tilde{\varepsilon}_Y^*$ and n :

$$\frac{P}{0.5\pi a^2 \sigma_Y} = 2\int_0^1 \tilde{\sigma}_{zz} \, d\tilde{r}^2 = F_p(n, \tilde{\varepsilon}_Y^*), \tag{16}$$

Eqs. (14) and (16) are two universal scaled functions depending on only two parameters $\tilde{\varepsilon}_Y^*$ and n.

The function F_d is the ratio of nominal radius a_i and contact radius a ($F_d = a_i/a$), which characterize the sinking-in and piling-up effects in the indentation (Fig. 3). The function F_p is twice the ratio of a mean contact stress ($P/\pi a^2$) and yield stress σ_Y. The explicit forms of F_d and F_p for general elasto-plastic materials are not available. For elastic deformation, the contact solutions can be obtained analytically (Sneddon, 1965) and F_d and F_p are found explicitly as

$$F_d = \pi/2, \quad F_p = 1/\tilde{\varepsilon}_Y^*. \tag{17}$$

To relate the F_d and F_p to the parameters C_d and C_p in CSM measurements, we assume that the CSM measurements are quasi-static. In this case there is a general relation between contact radius a and contact stiffness s (Cheng and Cheng, 1997; Dao et al., 2001)

$$s = 2a\beta E^*, \tag{18}$$

where β is a correction factor, which equals one for a small deformation solution (Sneddon, 1965) of an elastic material for any axisymmetric tip. Its value for general elasto-plastic solutions with large deformation is analyzed numerically in Section 5.2. Substituting Eq. (18) into Eq. (4) and comparing with Eqs. (14), (16), we obtain the relation between experimentally-measurable coefficients C_d, C_p and C in Eq. (4) and universal nondimensional functions F_d and F_p

$$C_d = \frac{1}{2\beta E^* \tan\theta} F_d(n, \tilde{\varepsilon}_Y^*), \tag{19a}$$

$$C_p = \frac{\pi\sigma_Y}{8\beta^2 E^{*2}} F_p(n, \tilde{\varepsilon}_Y^*). \tag{19b}$$

$$C = \frac{\pi\sigma_Y F_p(n, \tilde{\varepsilon}_Y^*)\tan^2\theta}{2F_d^2(n, \tilde{\varepsilon}_Y^*)}, \tag{19c}$$

One can also rewrite the coefficient C_p through the function $H(n, \tilde{\varepsilon}_Y^*, \sigma_Y) = P/\pi a^2 = \sigma_Y F_p(n, \tilde{\varepsilon}_Y^*)/2$, which becomes material hardness H when a plastic zone develops under an indenter

$$C_p = \frac{\pi}{4\beta^2 E^{*2}} H(n, \tilde{\varepsilon}_Y^*, \sigma_Y). \tag{19d}$$

Using scaling analysis, we obtained two universal nondimensional functions to determine the two independent parameters C_d and C_p measurable with the CSM nanoindentation test with sharp indenters. The scaling functions F_d and F_p have been obtained under the assumption of small deformation; the generality and validity of the scaled relations will be numerically validated in the next section using large deformation FEM computations.

4. FEM model

The explicit form of the scaling functions F_d and F_p cannot be obtained for general elasto-plastic materials. To relate these functions to material properties and tip geometry, comprehensive numerical simulations using finite element methods are performed and the analytical representation for these functions are obtained by fitting the simulated results. However the fitting function will satisfy asymptotic behavior for small and large $\tilde{\varepsilon}_Y^*$.

An axisymmetric finite element model with 6466 four-noded quadrilateral elements has been developed as shown in Fig. 4(a). The indenter cone is represented by an analytical rigid surface. The outside boundaries at the right and bottom of Fig. 4(a) are represented by infinite elements. All materials are modeled with the rate-independent von Mises yield plasticity model in ABAQUS® (version 6.4) with strain–stress relation defined by Eq. (2). Calculations are performed using the ABAQUS® large deformation option. In most of our cases the contact between indenter and substrate is frictionless; the effect of friction is discussed in Section 7.

To simulate the CSM measurements during indentation loading, the loading step is divided into several small substeps as shown in Fig. 4(b). Between two substeps, the linear perturbation procedure in ABAQUS® is inserted. In the linear perturbation step, the tip is excited with a 75 Hz (as in the experiment) vibration with 1 nm amplitude or applied 1 nm static displacement and the corresponding response force is calculated. The stiffness is the ratio of the response force and the applied displacement. Because the system resonance frequency is above 1 MHz when the tip is in contact with the material, while the driving frequency of CSM measurement is 45 Hz, the CSM measurement can be considered quasi-static. Our simulations show that the dynamic and static initial unloading stiffnesses are identical for the materials considered.

5. Numerical validation of the scaling relations

5.1. Displacement and load versus dynamic stiffness

Using the finite element model described in the previous section, comprehensive parametric studies have been performed for different materials and half apex angles. Fig. 5(a) shows the relation between displacement and stiffness and 5(b) between load and square of stiffness. All these relations can be linearly approximated, which agree with the scaling analysis based on the small deformation assumption. The computations have been performed for a conical indenter with 70.3° half apex angle. The 20 curves present results for 20 materials with different σ_Y/E ratios which vary linearly from 0.001 to 0.02 with a step of 0.001 (the lower limit is extended to 0.0001 in the next section). The modulus E is 100 GPa and Poisson ratio is 0.3; strain hardening exponent n is 0.2. For common engineering metals, the value for Young's modulus E varies between 10 and 210 GPa and yield stress σ_Y between 30 MPa and 3000 MPa (Bolshakov and Pharr, 1998; Dao et al., 2001) which gives for the σ_Y/E ratio range from 0.001 to 0.04. This corresponds to the range for the universal parameter $\tilde{\varepsilon}_Y^*(1/\tilde{\varepsilon}_Y^*)$ from 0.0028 (3580) to 0.1 (10) for a standard Berkovich indenter $\theta = 70.3°$. For example, for Al 2024 T3 ($E = 80$ GPa, $\sigma_Y = 350$ MPa), $\tilde{\varepsilon}_Y^*(1/\tilde{\varepsilon}_Y^*) = 0.0122(81.8)$.

5.2. The correction factor β

The factor β in Eqs. (18) and (19) is very important in calculating the contact area or modulus with known contact stiffness. Cheng and Cheng (1997) have shown that Eq. (18) with $\beta = 1$ is valid for materials with work hardening and residual stress under the assumption of infinitesimal deformation. Hay et al. (1999) showed that even for linear elastic materials, β is not unity for an indentation with a rigid cone if

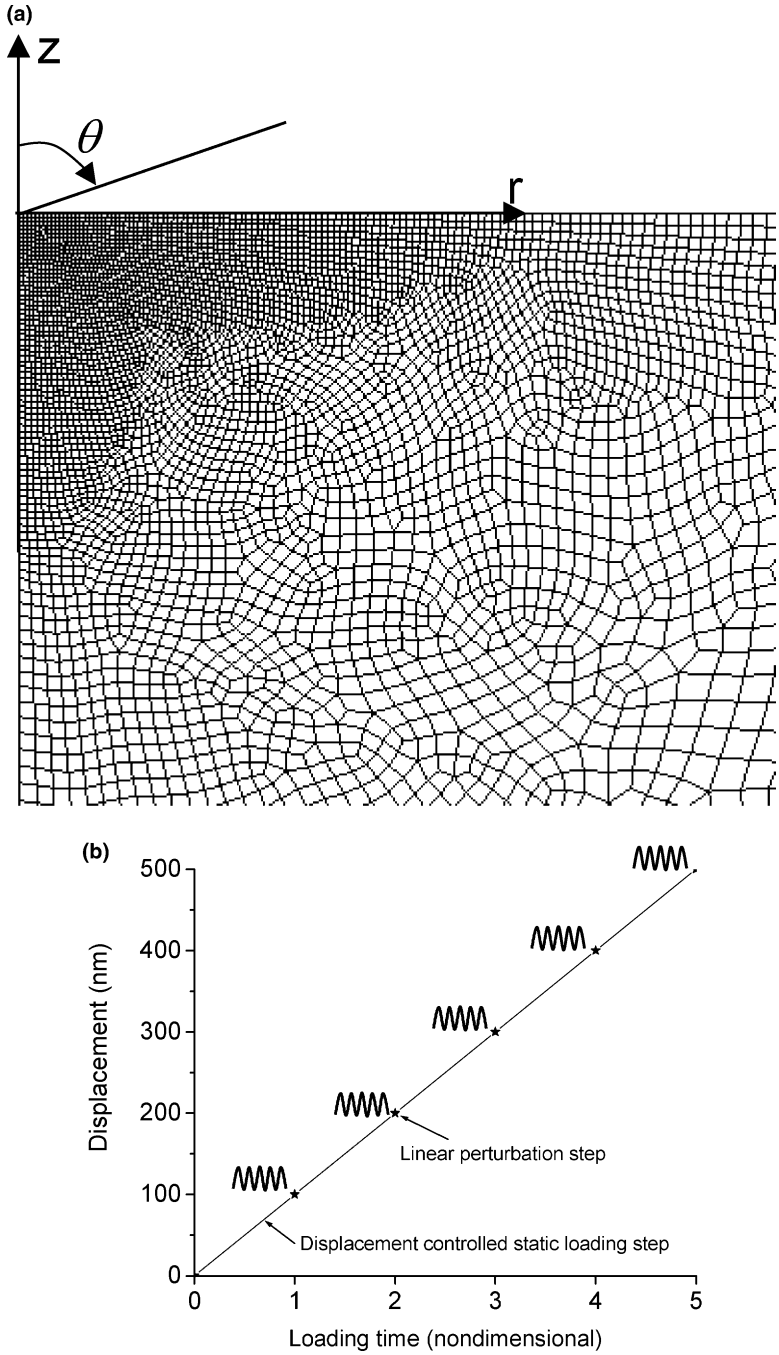

Fig. 4. Finite element model for a conical indenter. (a) Mesh design. The conical tip is represented by a rigid surface. (b) Schematic of load steps. The indentation is controlled by the displacement of the tip. The maximum displacement is 500 nm. The total load step is uniformly divided into substeps. At the end of each substep as indicated by stars, a linear perturbation analysis is performed to simulate the continuous stiffness measurement.

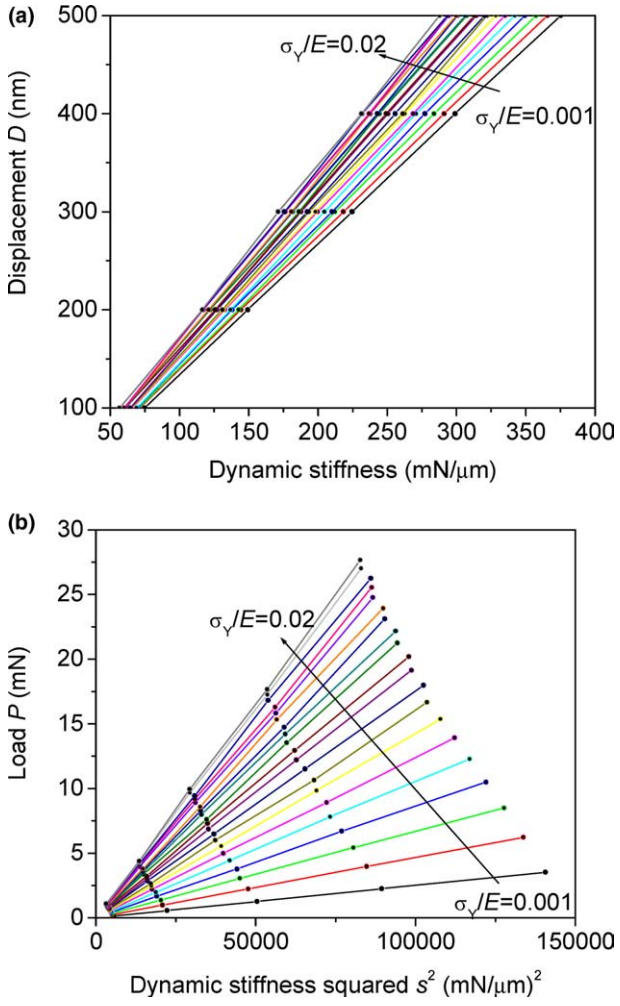

Fig. 5. Computation results for a conical indenter with half apex angle $\theta = 70.3°$; the materials have modulus $E = 100$ GPa and the σ_Y/E ratio increases linearly from 0.001 to 0.02 with a step of 0.001. (a) Relation between displacement and stiffness. (b) Relation between load and square of stiffness.

finite strain and rotation are considered. They showed that this is also because Sneddon's solution (1965) allows radial displacements in the contact region which does not conform to the boundary of the rigid cone. The approximate analytical equation given by Hay et al. (1999) shows that β depends on Poisson's ratio and the conic angle.

In the elasto-plastic regime, a wide range of βs have been reported. β has been calculated by Dao et al. (2001) to be 1.06 and by Cheng and Cheng (2000) to be between 1.06 and 1.11. A good review of the results of different authors for β is given by Oliver and Pharr (2004). To elucidate these differences in the β values, we have performed a systematic parametric study calculating the contact radius a at each perturbation step (Fig. 4) and computing, at the same indentation depth, the stiffness from the perturbation displacement and force. With the known modulus and Poisson's ratio, we have determined from Eq. (18) the correction factor β for various material properties and indenter cone angles θ as shown in Fig. 6. The dashed lines in Fig. 6 indicate the results calculated using Eq. (19) in Hay et al. (1999). As shown in Fig. 6, β is never unity from

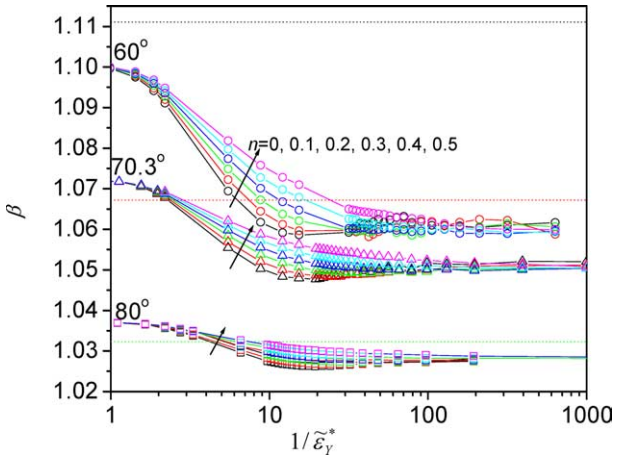

Fig. 6. Parameter β versus $\tilde{\varepsilon}_Y^*$. Poisson's ratio is 0.3. Three horizontal dotted lines are calculated using Eq. (19) in Hay et al. (1999).

the elastic to the fully plastic region and depends on cone angle θ and hardening exponent n and the extent of plasticity $\tilde{\varepsilon}_Y^*$. If FEM computations are performed in the small deformation approximation, β is close to 1.03 for all three cone angles (not shown in the figure). The deviation of β from unity is more significant for FEM computation with large deformations and rotation. As shown in Fig. 6, β varies with $1/\tilde{\varepsilon}_Y^*$. It has the largest value in the elastic region ($1/\tilde{\varepsilon}_Y^* < 1.0$) and decreases as $1/\tilde{\varepsilon}_Y^*$ increases. β has larger variation versus strain hardening exponent n at $1/\tilde{\varepsilon}_Y^*$ around 10 and approaches a constant for $1/\tilde{\varepsilon}_Y^*$ above 1000. In the elastic region ($1/\tilde{\varepsilon}_Y^* < 1.0$), it has reasonable agreement (within 1%) with the estimated values given by Hay et al. (1999). In both the elastic and full plastic regimes, it is almost independent of the strain hardening exponent n ; however it depends on n in the elasto-plastic region. The value of β also depends on the cone angle. For standard Berkovich indenters with effective cone angle 70.3°, one may select β to be 1.052 which is the average value in the full plastic region.

5.3. Universal scaling functions F_d and F_p

To further validate the universal scaling relation for F_d and F_p, we have performed a numerical parametric study of the F_d–$\tilde{\varepsilon}_Y^*$ and F_p–$\tilde{\varepsilon}_Y^*$ relations for various material properties and apex angles of indenters. For given indentation apex angle θ and material parameters E, ν and n, we have computed D–s and P–s^2 relations similar to Fig. 5, with linear increase of the σ_Y/E ratio from 0.001 to 0.02 with a step of 0.001. The coefficients C_d and C_p are found as slopes of the D-s and P–s^2 relations by least square linear fitting of the numerical data. Then from the C_d and C_p coefficients the two scaled functions F_d and F_p are calculated using Eq. (19). Figs. 7 and 8 show the effect of Young's modulus E and Poisson's ratio on the scaling relations. As shown in Figs. 7, 8, for $\nu = 0.3$, $n = 0.2$ and three different moduli $E = 30$, 100, 200 GPa, the scaled functions F_d and F_p are identical, i.e. the functions depend only on the parameter $\tilde{\varepsilon}_Y^*$ (10). For $E = 100$, $n = 0.2$, the scaled functions F_d and F_p are close for three different Poisson's ratios $\nu = 0.25$, 0.3, 0.35, indicating that its effect can be included using the reduced modulus, and in the following analysis we select $\nu = 0.3$. Figs. 9 and 10 plot the scaled relations for three different half apex angles ($\theta = 60°$, 70.3°, 80°) for different strain hardening exponents n. They show the scaled functions are universal over apex angle.

Figs. 7–10 demonstrate numerically, in the regime of large deformation, the validity of universal properties of the scaling functions, although they were obtained using small deformation analysis. The scaled function F_d is similar to the surface profile parameter γ_1 defined by Sakai et al. (2004) who also numerically

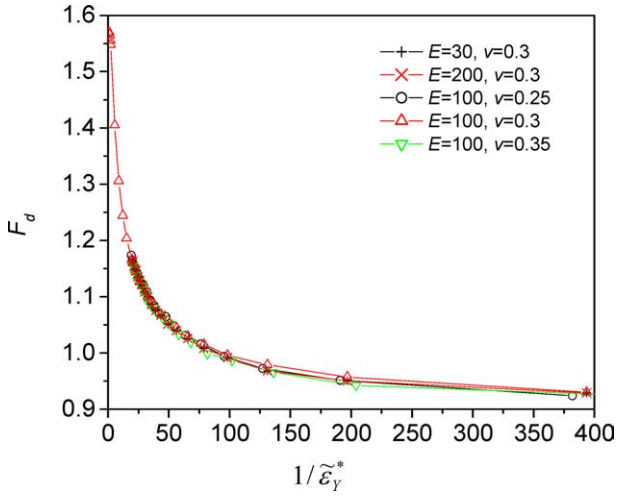

Fig. 7. Effect of Young's modulus E and Poisson's ratio on the scaling relation between F_{d} and $\tilde{\varepsilon}^{*}_{\mathrm{Y}}$. The strain hardening exponent is 0.2.

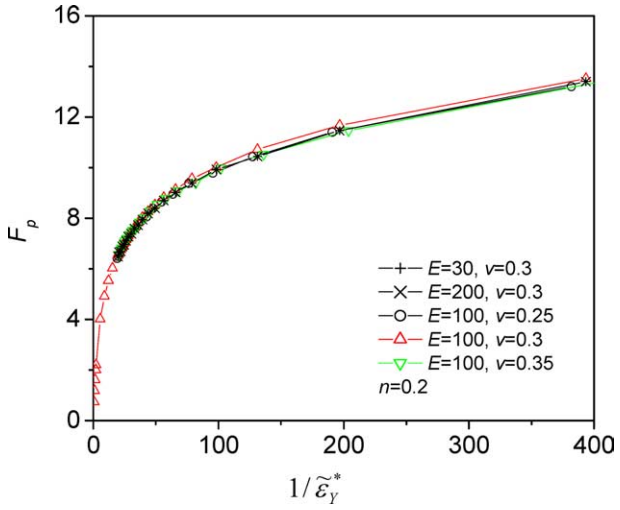

Fig. 8. Effect of Young's modulus E and Poisson's ratio on the scaling relation between F_{p} and $\tilde{\varepsilon}^{*}_{\mathrm{Y}}$. The strain hardening exponent is 0.2.

demonstrated the universality of this scaled function over the apex angle for elasto-plastic materials with linear strain-hardening. The parameter $C/\tan^2\theta$ (Eq. (19c)) is also a universal function over the apex angle; this fact has also been approximately verified by Bucaille et al. (2003).

6. Explicit representation of the scaling functions

In the previous section, using finite element simulation, we have verified the generality of the scaled formulation F_{d}, F_{p}. However, the exact analytical formulations for these functions cannot be obtained in the

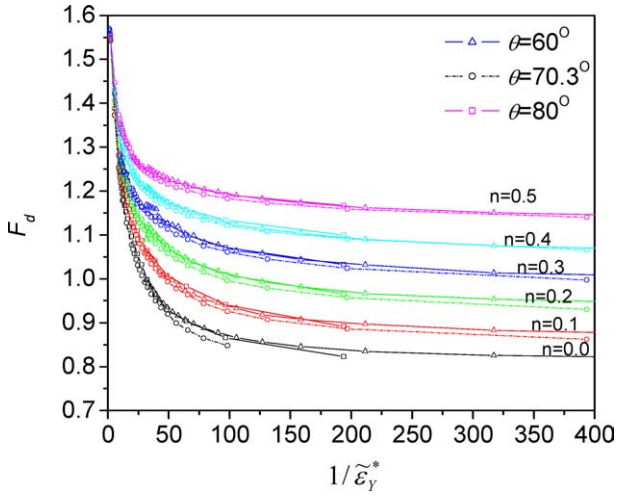

Fig. 9. Effect of apex angle on the scaling relation between F_d and $\tilde{\varepsilon}^*_Y$ for different strain hardening exponents n.

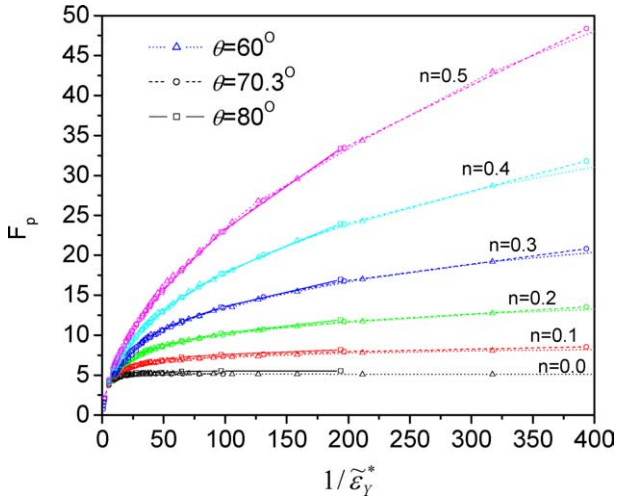

Fig. 10. Effect of apex angle on the scaling relation between F_p and $\tilde{\varepsilon}^*_Y$ for different strain hardening exponents n.

general case of elasto-plastic materials. Here we obtain these functions by fitting the numerical results and then use the asymptotic behavior of the solutions for small and large $\tilde{\varepsilon}^*_Y$. To analyze F_d, F_p versus $\tilde{\varepsilon}^*_Y$ we plot them for different ns in a log/log scale. We have selected a very large range of $\tilde{\varepsilon}^*_Y$ to demonstrate their asymptotic behavior in Figs. 11 and 12.

6.1. Asymptotic behavior at small and large $\tilde{\varepsilon}^*_Y$

At small $1/\tilde{\varepsilon}^*_Y$ (less than 1.0), F_d approaches the elastic solution: $F_d = F^0_d = \pi/2$ (Fig. 11); this condition corresponds to σ_Y approaching infinity. For incompressible materials ($\nu = 0.5$), yield will initiate only at the apex angles of the indenter when $1/\tilde{\varepsilon}^*_Y > 1$ (Johnson, 1985) while for compressible material, plastic flow initiates for any value of $\tilde{\varepsilon}^*_Y$ but is small for large $\tilde{\varepsilon}^*_Y$. For F_p, in the elastic regime the numerical result based on

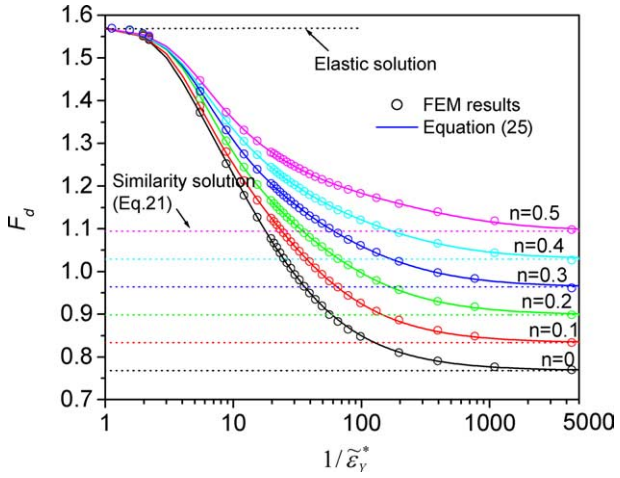

Fig. 11. Relation between F_d and $\tilde{\varepsilon}_Y^*$.

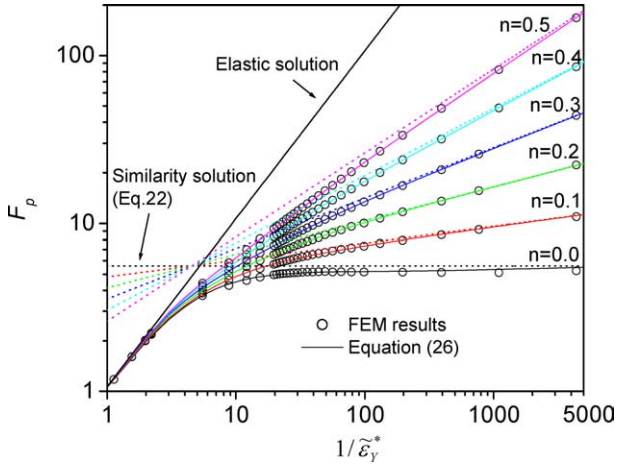

Fig. 12. Relation between F_p and $\tilde{\varepsilon}_Y^*$.

large deformation is slightly larger than from Sneddon's elastic solution ($F_p = 1/\tilde{\varepsilon}_Y^*$, Eq. (17)) as has been discussed by Hay et al. (1999). Based on the analysis for parameter β in Section 5.2, F_p may be represented as

$$F_p = F_p^0 = \beta_e/\tilde{\varepsilon}_Y^*, \tag{20}$$

where β_e corresponds to the elastic limit of β at $1/\tilde{\varepsilon}_Y^* < 1$ (Fig. 6).

As $(1/\tilde{\varepsilon}_Y^*)$ increases, the contribution of plasticity increases (σ_Y decreases), and F_d decreases and for a given strain hardening exponent n approaches a constant F_d^∞. In the full plasticity limit, F_d^∞ depends only on the strain hardening exponent n. Based on the numerical results at the full plastic range at $(1/\tilde{\varepsilon}_Y^*) = 4395.6$ shown in Fig. 13(a), it is found that F_d^∞ can be approximated as a linear function of n as

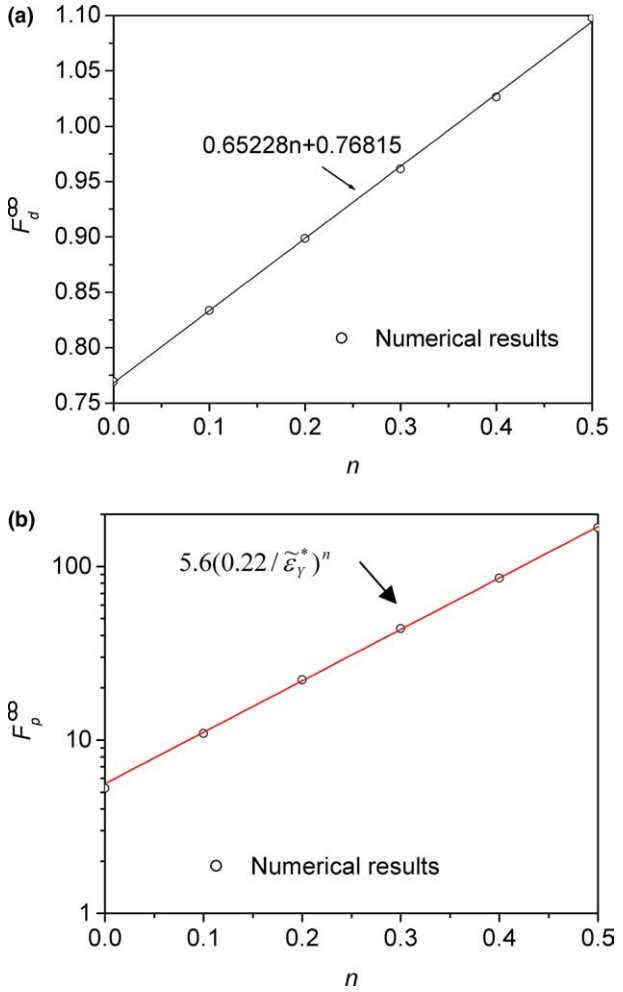

Fig. 13. Results in full plastic regime. The open circles are numerical results at $1/\tilde{\varepsilon}_{\mathrm{Y}}^* = 4395.60$. The solid lines show the fittings (Eqs. (21) and (22)). (a) F_{d}^{∞} versus n. (a) $\log(F_{\mathrm{p}}^{\infty})$ versus n. Both relations are approximately linear.

$$F_{\mathrm{d}}^{\infty} = 0.6523n + 0.7682. \tag{21}$$

The value of $F_{\mathrm{d}} = \mathrm{a}_i/a$ (see Fig. 3) is important to distinguish the indentation status with material "sinking-in" or "piling-up". For small $(1/\tilde{\varepsilon}_{\mathrm{Y}}^*)$, F_{d} is larger than one ($a_i > a$) which corresponds to "sinking-in" of the deformed surface profile (see Fig. 3b). As $(1/\tilde{\varepsilon}_{\mathrm{Y}}^*)$ increases, F_{d} may become less than one ($a_i < a$) which corresponds to "piling-up" of the deformed surface profile (Fig. 3a). The transition value of $1/\tilde{\varepsilon}_{\mathrm{Y}}^*$ from "sinking-in" to "piling-up" depends on the strain hardening exponent n. The larger n is the larger is the transition value of $1/\tilde{\varepsilon}_{\mathrm{Y}}^*$. From Eq. (21), one obtains that when $n > 0.35$, F_{d} is always larger than one and therefore only "sinking in" behavior is observed even for large $1/\tilde{\varepsilon}_{\mathrm{Y}}^*$.

Fig. 12 represents the F_{p}–$\tilde{\varepsilon}_{\mathrm{Y}}^*$ relations, F_{p} approaches the elastic solution ($F_{\mathrm{p}} = \tilde{\varepsilon}_{\mathrm{Y}}^*$) at small $1/\tilde{\varepsilon}_{\mathrm{Y}}^*$. In the full plastic regime (large $1/\tilde{\varepsilon}_{\mathrm{Y}}^*$), in a log-log scale F_{p} has a linear relation with $1/\tilde{\varepsilon}_{\mathrm{Y}}^*$. Therefore in this range F_{p} can be represented as a power function of $(1/\tilde{\varepsilon}_{\mathrm{Y}}^*)$ (Fig. 13b)

$$F_{\mathrm{p}}^{\infty} = 5.6(0.22/\tilde{\varepsilon}_{\mathrm{Y}}^*)^n. \tag{22}$$

From Eqs. (19b) and (19d) we can obtain the relation between F_p and hardness H: $F_p = 2H/\sigma_Y$ and rewrite Eq. (22) as

$$H = 2.8\sigma_r^T, \tag{23}$$

where $\sigma_r^T = \sigma_Y(\frac{E}{\sigma_Y}\varepsilon_r^T)^n$ is the representative flow stress and ε_r^T is the Tabor's representative plastic strain which is obtained as

$$\varepsilon_r^T = \frac{0.22}{(1-\nu^2)\tan\theta}. \tag{24}$$

For the Berkovich indenter ($\theta = 70.3°$), ε_r^T equals 8.65% for $\nu = 0.3$. From analysis of the available experimental data Tabor (1951) has found that the hardness value is about three times σ_r at a representative strain ε_r^T of 8–10%. Numerical simulations given by Cheng and Cheng (2000) show $H = 2.8\sigma_r^T$ at representative strain $\varepsilon_r^T = 10\%$. Larsson (2001) and Mata et al. (2002) numerically obtained similar results. In general, according to Johnson (1985) the representative strain ε_r^T is expressed as $0.2/\tan\theta$. Thus the relation (22) is in good agreement with experimental results and other numerical simulations.

6.2. Arbitrary $\tilde{\varepsilon}_Y^*$

The explicit representations for F_d and F_p in a whole range of the parameter $1/\tilde{\varepsilon}_Y^*$ are obtained by fitting the numerical results (shown in Figs. 12 and 13 by solid lines). We select fitting functions in such a way that they asymptotically converge to the elastic solution when the yield stress approaches infinity (small $1/\tilde{\varepsilon}_Y^*$) and to the similarity solution when the yield stress approaches zero (large $1/\tilde{\varepsilon}_Y^*$). Based on these criteria and the behavior of F_d and F_p shown in Figs. 12 and 13, we select F_d, F_p as

$$F_d = \frac{\pi}{2} + \left(F_d^\infty - \frac{\pi}{2}\right) W_d(n, \tilde{\varepsilon}_Y^*), \tag{25}$$

$$F_p = \frac{1}{\frac{1}{F_p^0} + \frac{1}{F_p^\infty} W_p(n, \tilde{\varepsilon}_Y^*)}, \tag{26}$$

where $W_d(n, \tilde{\varepsilon}_Y^*)$ and $W_p(n, \tilde{\varepsilon}_Y^*)$ are two weighting functions, which equal one when $\tilde{\varepsilon}_Y^*$ is zero and equal zero as $\tilde{\varepsilon}_Y^*$ approaches infinity. We have selected $W_d(n, \tilde{\varepsilon}_Y^*)$ and $W_p(n, \tilde{\varepsilon}_Y^*)$ in the form

$$W_d = \frac{1 + M_3\tilde{\varepsilon}_Y^*}{1 + M_4\tilde{\varepsilon}_Y^* + M_2\tilde{\varepsilon}_Y^{*2} + M_1\tilde{\varepsilon}_Y^{*4}} \quad \text{and} \quad W_p = \frac{1 + N_3\tilde{\varepsilon}_Y^*}{1 + N_4\tilde{\varepsilon}_Y^* + N_2\tilde{\varepsilon}_Y^{*2} + N_1\tilde{\varepsilon}_Y^{*4}}, \tag{27}$$

where the parameters M_i and $N_i (i = 1, \ldots 4)$ are polynomial functions of n; their coefficients are determined by least square minimization of the deviation of the fitting functions from the numerical results:

$$\begin{aligned} M_1 &= 4029085.1n^4 - 3433399.5n^3 + 1002412.7n^2 - 49901.37n + 236.26, \\ M_2 &= 83651.34n^4 - 63538.0n^3 + 21664.08n^2 - 1086.89n + 8.24199, \\ M_3 &= 13356.83n^4 - 10190.15n^3 + 3047.238n^2 - 131.8854n - 0.84493, \\ M_4 &= 16465.49n^4 - 12513.71n^3 + 3636.994n^2 - 136.5563n + 10.29702, \end{aligned} \tag{28a}$$

$$\begin{aligned} N_1 &= -1369.298n^4 + 2107.555n^3 + 7844.612n^2 - 7387.781n + 1677.144, \\ N_2 &= 137303.3n^4 - 160219.3n^3 + 104661.2n^2 - 44535.86n + 8131.09, \\ N_3 &= 11343.12n^4 - 16468.55n^3 + 17429.03n^2 - 9429.969n + 1810.06, \\ N_4 &= 3547692.0n^4 - 2590250n^3 + 394978.0n^2 - 11831.79n + 23219.68. \end{aligned} \tag{28b}$$

The results calculated by Eqs. (25)–(28) are shown by solid lines in Figs. 11 and 12. The numerical results obtained for 70.3° apex angle are shown by open circles. The full plastic solutions (21), (22) are indicated by dotted lines.

6.3. Relation between scaling functions F_d, F_p and $\Pi_{1\theta}$, $\Pi_{2\theta}$

The scaling functions F_{d} and F_{p} are formulated to describe continuous stiffness measurements. But because for metals the CSM measurement can be considered as quasi-static, the dynamic stiffness equals the local unloading stiffness at the same indentation depth. Furthermore for homogeneous materials the relation between stiffness s and indentation depth D is linear. Thus if the unloading stiffness at maximum indentation depth as shown in Fig. 1 is given, the dynamic stiffness at all indentations as shown in Fig. 2b is also determined. Therefore one can relate F_{d} and F_{p} to the scaling functions $\Pi_{1\theta}$ and $\Pi_{2\theta}$ using Eq. (3) given by Dao et al. (2001) which are based on the unloading stiffness at a specific indentation depth. The relation between (F_{d}, F_{p}) and ($\Pi_{1\theta}$, $\Pi_{2\theta}$) is obtained by comparing Eq. (3) and Eqs. (14), (16) and (18):

$$F_{\mathrm{d}} = \frac{2\beta \tan\theta}{\Pi_{2\theta}}, \tag{29}$$

$$F_{\mathrm{p}} = \frac{8\Pi_{1\theta}\beta^2\sigma_{\mathrm{r}}}{\pi\Pi_{2\theta}^2\sigma_{\mathrm{Y}}}. \tag{30}$$

Fig. 14 compares the results for F_{p} computed at $\theta = 70.3$ using Eq. (30) with the use of functions $\Pi_{1\theta}$, $\Pi_{2\theta}$ from Dao et al. (2001) (shown by dotted lines) and that using Eqs. (26) and (27) (solid lines). The two solutions are very close within the elastic–plastic regime ($10 < 1/\tilde{\varepsilon}_{\mathrm{Y}}^{*} < 200$). However, because the empirical functions obtained by Dao et al. (2001) are based on fitting by polynomials in a limited range of $\ln(E^*/\sigma_{\mathrm{r}})$ without taking into account the explicit solutions for elastic and full plastic regimes, they do not obey the asymptotic properties of the exact solution and are not applicable for the elastic and full plastic regimes. For example, when E^*/σ_{r} approaches zero (elastic solution), an empirical function in the form of polynomials of $\ln(E^*/\sigma_{\mathrm{r}})$ approaches infinity. As shown in Fig. 14 by the dotted lines, F_{p} calculated using

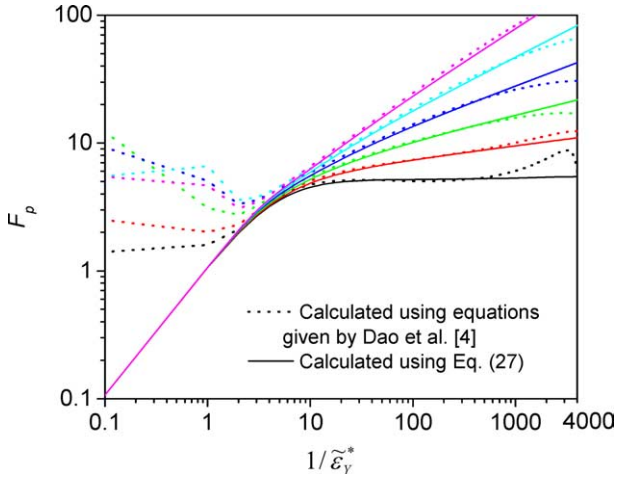

Fig. 14. F_{p} computed using Eq. (30) with the empirical equations for $\Pi_{1\theta}$, $\Pi_{2\theta}$ given by Dao et al. (2001) (dotted lines) and F_{p} computed using Eq. (26) (solid lines).

$\Pi_{1\theta}$, $\Pi_{2\theta}$ empirical functions does not follow the elastic solution (linear relation with $1/\tilde{\varepsilon}^*_Y$) at small $\tilde{\varepsilon}^*_Y (< 1)$. Further the scaled functions F_d, F_p are universal over apex angle while $\Pi_{1\theta}$, $\Pi_{2\theta}$ depend on θ.

7. Effect of friction on scaling functions F_d, F_p

It has been observed that the friction on the interface between a sharp indenter and a substrate has significant effect on the plastic flow in the vicinity of the indenter and in particular on the material "piling-up" (Bucaille et al., 2003; Mata and Alcalá, 2004). To account for the friction effect on the scaling functions F_d, F_p, we computed those functions using the FEM model described in Section 4 with various friction coefficients μ between the indenter and substrate surfaces.

Let us first consider the full plastic regime. The computed results at $1/\tilde{\varepsilon}^*_Y = 4395.6$ are shown in Fig. 15 by open symbols. Considering that a smaller cone angle has more significant influence of friction, as suggested by Johnson (1985), Bucaille et al. (2003) and Mata and Alcalá (2004), we use the parameter $\mu \cot\theta$ to

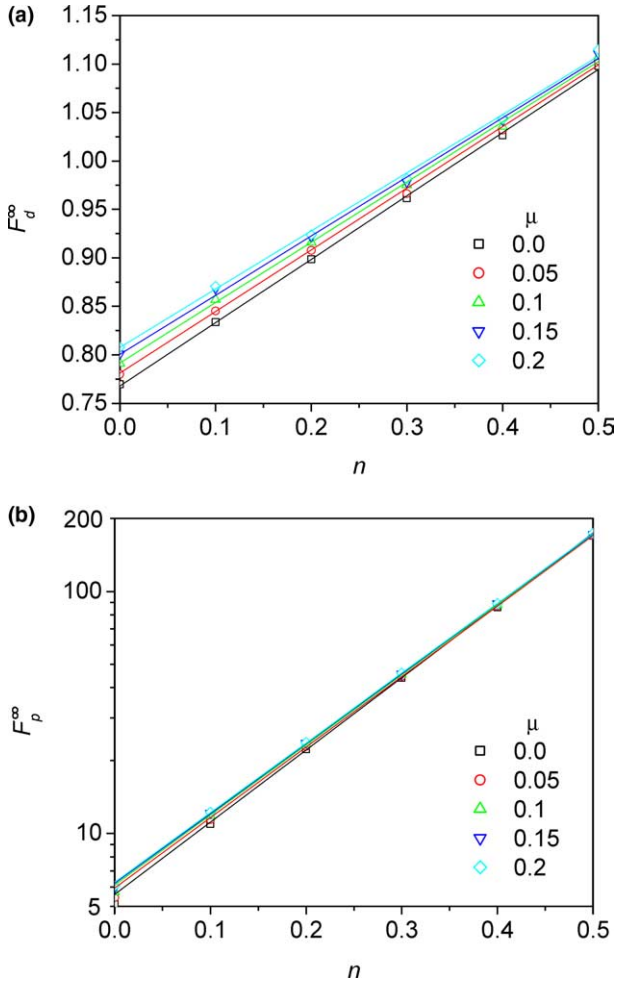

Fig. 15. Effect of contact friction on the scaling functions in full plastic regime at $1/\tilde{\varepsilon}^*_Y = 4395.6$ for $q = 70.3°$. FEM computations are given by points. Lines are Eqs. (31) and (32) with coefficients (33). (a) F_d^∞, (b) F_p^∞.

account for the influence of cone angle θ. To qualitatively describe the friction effect, we fit the numerical results in the full plastic regime in Fig. 15 by modifying the functions F_{d}^{∞}, F_{p}^{∞} Eqs. (21), (22) as:

$$F_{\mathrm{d}}^{\infty} = C_1(\mu\cot\theta)n + C_2(\mu\cot\theta), \tag{31}$$

$$F_{\mathrm{p}}^{\infty} = C_3(\mu\cot\theta)(C_4(\mu\cot\theta)/\tilde{\varepsilon}_{\mathrm{Y}}^{*})^{n}, \tag{32}$$

where the coefficients C_i $(i = 1,2,3,4)$ are functions of the parameter $\mu\cot\theta$. The numerical results are calculated for $\theta = 70.3°$ and for this case the coefficients C_i in (32), (31) are obtained after fitting optimization as

$$\begin{aligned} C_1 &= 0.481 + 0.172/(1.0 + 6.151\mu\cot\theta),\\ C_2 &= 0.891 - 0.123/(1.0 + 6.671\mu\cot\theta),\\ C_3 &= 6.593 - 0.995/(1.0 + 30.2\mu\cot\theta),\\ C_4 &= 0.1665 + 0.0535/(1.0 + 93.79\mu\cot\theta). \end{aligned} \tag{33}$$

The fitting results are represented by the solid lines in Fig. 15.

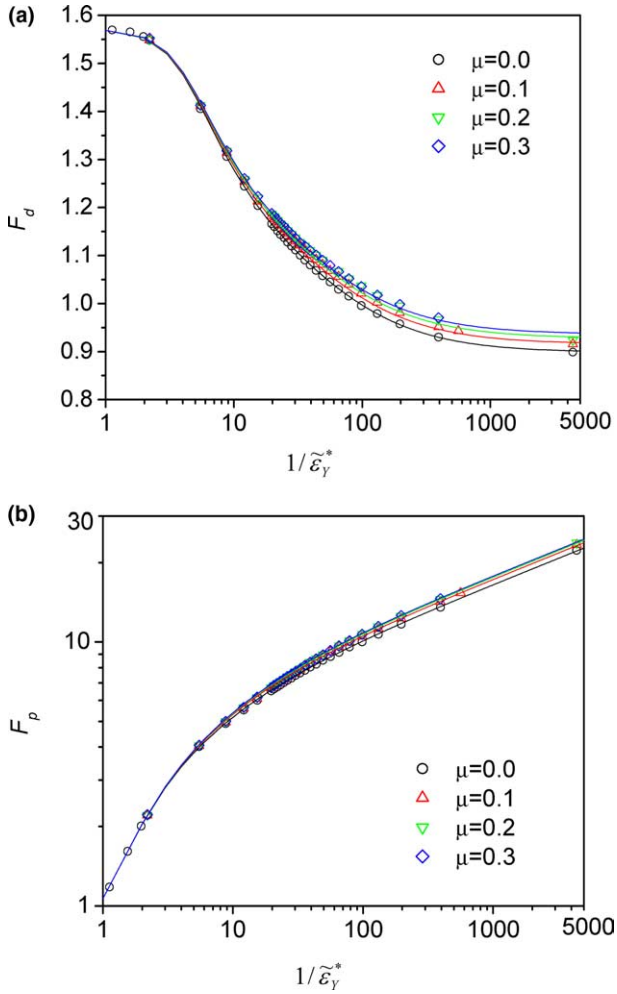

Fig. 16. Effect of contact friction on the scaling functions at $\theta = 70.3°$, $n = 0.2$. Points are the FEM results; curves are computed using Eqs. (25) and (26), with F_{d}^{∞}, F_{p}^{∞} given by Eqs. (31) and (32). (a) F_{d}, (b) F_{p}.

Fig. 16 shows the numerical results (open symbols) versus parameter $1/\tilde{\varepsilon}_Y^*$ in the whole elasto-plastic range for four different friction coefficients $\mu = 0$, 0.1, 0.2, 0.3; the results are for a standard Berkovich indenter with $\theta = 70.3°$ and work hardening exponent $n = 0.2$. As shown in Fig. 15, both F_d, F_p increase as friction μ increases. The friction effect reduces the contact area and diminishes the material "piling-up". The effect becomes more significant as the plasticity contribution $1/\tilde{\varepsilon}_Y^*$ increases. Since in the elastic regime, the friction effect is negligible and more pronounced for large $1/\tilde{\varepsilon}_Y^*$, to account for it and to obtain general formulations for F_d and F_p in the presence of friction we have substituted the full plastic solutions with friction Eqs. (31), (32) into Eqs. (25), (26). The comparison between these general formulations with numerical results are given in Fig. 16, where such computed F_d and F_p functions are shown by solid lines.

8. Applicability of scaling functions F_d, F_p for general uniaxial stress–strain relations

As discussed in previous sections, the analysis is based on the stress–strain relation approximated by the piecewise-linear/power-law function (2). Although this relation has been widely used in simulation of nanoindentation responses (Cheng and Cheng, 1998, 2000; Dao et al., 2001; Bucaille et al., 2003; Mata and Alcalá, 2004), the experimental uniaxial stress–strain relation can be much more complicated and the stress–strain relation cannot always be well represented by Eq. (2) with three variables (E, σ_Y and n), which reduce after scaling to two independent parameters ($\tilde{\varepsilon}_Y^*$, n). For example for some ferritic steels, the strain–stress relation has two distinct regions with different strain-hardening exponents n (Umemoto et al., 2000). In these cases, the stress–strain relation has to be approximated by a model with more than three variables, which cannot be scaled to the model described by only two parameters. Thus in this case the universal functions F_d and F_p cannot be represented in the same form of Eqs. (25) and (26). However, the loading response and the initial unloading slope in nanoindentation tests with sharp indenters are described by two parameters (C_d, C_p) (Eq. (4)). Thus the stress–strain relation which has three or more independent parameters is not uniquely related to the indentation response described by only two independent parameters.

Significant effort has been put forward in the past to relate hardness to constitutive properties of materials. As follows from Eq. (23), in the full plasticity range, as was suggested by Tabor (1951), the material hardness is dependent on only one parameter: representative stress σ_r. In the spherical cavity model proposed by Johnson (1970, 1985) the hardness is represented using Tabor's representative stress σ_r and scaling parameter $\tilde{\varepsilon}_Y^*$. Larsson et al. (1996) and Larsson (2001) have demonstrated that the FEM calculated and experimental hardness data are better approximated by the Johnson model when two representative stresses are used. By FEM analysis, Larsson (2001) has shown that material having different irregular stress–strain curves which have the same two representative stresses at representative strains 2% and 35% have the same hardness.

In this section we will compare the indentation responses for different stress–strain relations which do not obey the power law (2). Following Larsson (2001) all of them will have the same stress at two representative strains (2% and 35%). One can always select uniquely the equivalent (representative) power law stress–strain function (2) passing through the same representative stresses. The equivalent materials will have the same Young's modulus, as the original materials with more general stress–strain curves, and equivalent σ_Y^E and n^E. In this case, using these equivalent parameters one can use the universal functions F_d and F_p represented by Eqs. (25), (26) to predict indentation response which will be compared to those calculated by FEM for materials with selected general stress–strain relations.

To investigate the applicability of the universal functions F_d and F_p to materials with more complicated stress–strain relations, let us first consider a more general stress–strain representation

$$\sigma = \begin{cases} E\varepsilon, & \sigma < \sigma_1, \\ \sigma_1 + \sigma_0 \varepsilon_p^{1/m}, & \sigma \geqslant \sigma_1, \end{cases} \tag{34}$$

where ε_p is plastic strain, E, σ_1, σ_0 and m are four independent parameters (the total strain ε is the summation of the plastic ε_p and elastic σ/E strains). The scaled stress–strain relation of Eq. (34) can not be reduced to two independent parameters as in Eq. (2). For a material with stress–strain relations described by Eq. (34) with a given set of parameters E, σ_1, σ_0 and m, the stresses at 2% and 35% representative plastic strains are determined and the equivalent material parameters E, σ_Y^E and n^E in Eq. (2) are selected to obtain the same stresses at those representative plastic strains. As an example, Fig. 17 shows as a solid line the stress–plastic strain relation calculated using Eq. (34) with $\sigma_1 = 1.0$ GPa, $\sigma_0 = 0.5$ GPa and $m = 3.3$ and the corresponding power-law relation (2) ($\sigma_Y^E = 1.0429$ GPa and $n^E = 0.0637$) is shown by a dotted line, which has identical stresses at 2% and 35% plastic strains. The "exact" indentation response for the stress–plastic strain relation (34) (the solid line in Fig. 17) is calculated using FEM and plotted as dotted lines in Fig. 18 for two materials with modulus $E = 100$ GPa and 200 GPa respectively. The Poisson's ratio is 0.3 and the half angle of the sharp indenter is 70.3°. Using the equivalent power-law relation (the solid line in Fig. 17), the "approximate" indentation response using the scaling functions is calculated: first one calculates F_d and F_p by substituting E, σ_Y^E and n^E into Eqs. (25), (26), then computes the indentation response C_d and C using Eqs. (29a,c). With the parameter C we obtain the loading response $P = CD^2$ and with the parameter C_d, we obtain the unloading slope $s = U_{max}/C_d$ at indentation depth U_{max}. The "approximate" indentation responses are plotted as solid lines in Fig. 18. Comparing the "exact" (solid lines) and "approximate" (dotted lines) in Fig. 18, we can see, using two representative plastic strains, that the scaling functions are applicable to computing the indentation response for materials with more general stress–strain relation.

To investigate the sensitivity of the scaling functions to different types of stress–strain relations, we have used five stress–plastic strain curves shown in Fig. 19. The 4th curve is calculated using Eq. (34) with $\sigma_1 = 1.0$ GPa, $\sigma_0 = 1.5$ GPa and $m = 3.3$. The irregular stress–strain curves 1–3 are represented using piecewise-linear functions. The power-law approximation (2) has yield stress $\sigma_Y^E = 1.184$ GPa and $n^E = 0.139$ and is plotted as a dotted line in Fig. 19. All the relations have the same stresses at 2% and 35% plastic strains and the elastic modulus is 200 GPa and Poisson's ratio is 0.3. The "exact" indentation responses for the four nonpower-law stress–strain relations given in Fig. 19 are computed using FEM and plotted as symbols

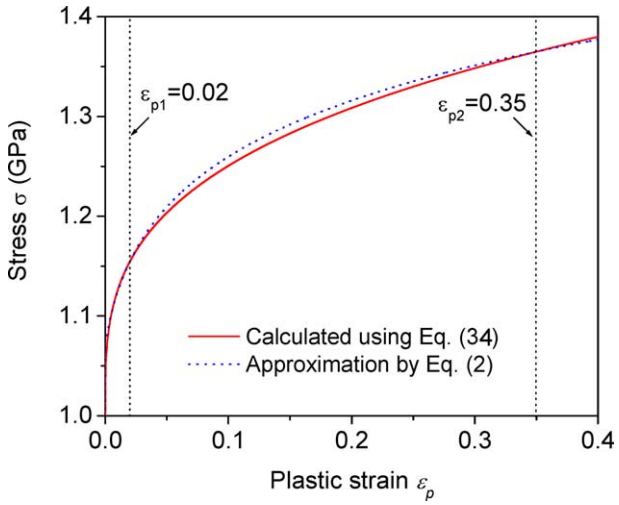

Fig. 17. Approximation of the stress–strain relation (34) (solid line) by the power-law function (2) (dotted line). The equivalent power law function parameters (σ_Y^E and n^E) are selected such that the stresses for both functions are equal at two representative plastic strains 2% and 35%.

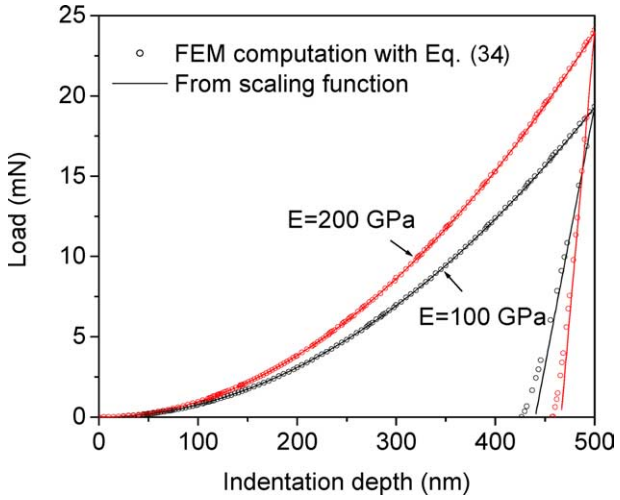

Fig. 18. Comparison of indentation responses calculated using stress–strain relations (2) and (34) for materials with two different Young's moduli (100 and 200 GPa). Open circles are FEM simulations with the stress–plastic strain relation given by the solid line in Fig. 17. The solid lines are calculated using the scaling functions (Eqs. (25), (26) and (19a,c)) with the approximated power law stress–strain relation (2); for unloading only initial unloading slope S is shown by the straight solid line.

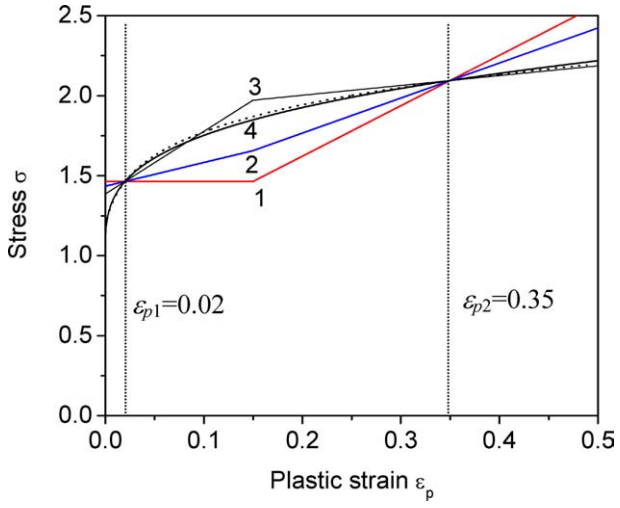

Fig. 19. Stress–strain relations with different degrees of deviation from the power-law approximation Eq. (2) (dotted line). Stress–strain relation 4 is calculated using Eq. (34). Relations 1–3 are represented by piecewise-linear functions. All stress–strain curves have the same stresses at 2% and 35% plastic strains.

in Fig. 20. The indentation response for the approximated power-law relation is calculated using scaling functions and is plotted as a solid line in Fig. 20. One can see that the irregularity of the stress–strain relations has little effect on the indentation response as long as all have the same stress at two representative strains. Therefore the indentation response for those relations can be well described by the scaling functions derived from the equivalent power-law relation.

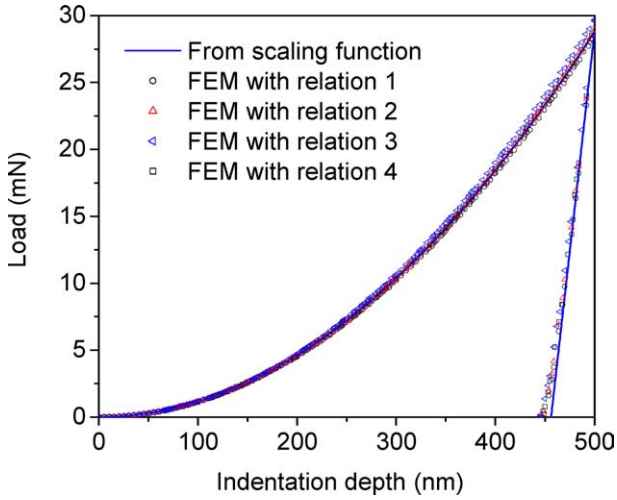

Fig. 20. Calculated loading/unloading indentation cycles using the stress–strain relations given in Fig. 19, Young's modulus is 200 GPa. The results (symbols) for nonpower-law relations 1–4 are calculated using FEM. The solid line is for the power-law relation; it is calculated using the scaling functions (Eqs. (25), (26) and (19a,c)); for unloading only initial unloading slope S is shown by the straight solid line.

9. Conclusions

Using scaling analysis, two universal functions which relate the two independent parameters (slope of the D–s and P–S^2) in the CSM nanoindentation measurement to the material elasto-plastic properties have been obtained. For materials with power-law strain hardening behavior the scaled functions reduce the number of the governing parameters from five (apex angle θ and four material properties E, ν, n, σ_Y) to only two nondimensional parameters $(n, \tilde{\varepsilon}_Y^*)$. The finite element method with linear dynamic and static perturbation is used to simulate CSM nanoindentation and verify the universality of the functions. Explicit equations for the universal scaled functions have been obtained by fitting the numerical results with and without friction. The explicit solutions asymptotically approach the elastic solution at a low plasticity state and the full plastic solution at a high plasticity state and are thus valid for arbitrary elasto-plastic states of the materials with power-law strain hardening behavior. The simple solution has advantages for inversion of the data in CSM nanoindentation measurements. The practical usefulness of the scaling functions for nonpower-law stress–strain relations has been addressed. The important conclusion is that materials with different nonpower and power-law uniaxial stress–strain curves have almost identical indentation responses as long as the stress–strain curves have the same stresses at two representative strains: 2% and 35%. Therefore the indentation response can be well described by the scaling functions derived from the equivalent power-law function which is selected to pass through the same two representative strains.

Acknowledgments

The research was partially sponsored by the Federal Aviation Administration (FAA) under contract No. 97-C001, and by the USAF Research Laboratory under contract F33615-03-D5204 through Universal Technology Corporation (UTC). The authors appreciate Mr. Moshe Ganor performing the nanoindentation measurements shown in Fig. 2.

References

Bhattacharya, A.K., Nix, W.D., 1988. Finite element simulation of indentation experiments. Int. J. Solids Struct. 24, 881–891.

Bucaille, J.L., Stauss, S., Felder, E., Michler, J., 2003. Determination of plastic properties of metals by instrumented indentation using different sharp indenters. Acta Mater. 51, 1663–1678.

Bolshakov, A., Pharr, G.M., 1998. Influences of pileup on the measurement of mechanical properties by load and depth sensing indentation techniques. J. Mater. Res. 13, 1049–1058.

Cheng, C.M., Cheng, Y.T., 1997. On the initial unloading slope in indentation of elastic–plastic solids by an indenter with an axisymmetric smooth profile. Appl. Phys. Lett. 71, 2623–2625.

Cheng, Y.T., Cheng, C.M., 1998. Scaling approach to conical indentation in elastic–plastic solids with work hardening. J. Appl. Phys. 84, 1284–1291.

Cheng, C.M., Cheng, Y.T., 1999. Can stress–strain relationships be obtained from indentation curves using conical and pyramidal indenters? J. Mater. Res. 14, 3493–3496.

Cheng, Y.T., Cheng, C.M., 2000. What is indentation hardness? Surf. Coat. Technol. 133, 417–424.

Chollacoop, N., Dao, M., Suresh, S., 2003. Depth-sensing instrumented indentation with dual sharp indenters. Acta Mater. 51, 3713–3729.

Constantinescu, A., Tardieu, N., 2001. On the identification of elastoviscoplastic constitutive laws from indentation tests. Inverse Prob. Eng. 9, 19–44.

Dao, M., Chollacoop, N., Van Vliet, K.J., Venkatesh, T.A., Suresh, S., 2001. Computational modeling of the forward and reverse problems in instrumented sharp indentation. Acta Mater. 49, 3899–3918.

Doerner, M.F., Nix, W.D., 1986. A method for interpreting the data from depth-sensing indentation instruments. J. Mater. Res. 1, 601–613.

Fischer-Cripps, A.C., 2002. In: NanoindentationMechanical Engineering Series. Springer-Verlag.

Giannakopoulos, A.E., Suresh, S., 1999. Determination of elastoplastic properties by instrumented sharp indentation. Scripta Mater. 40, 1191–1200.

Hay, J.C., Bolshakov, A., Phar, G.M., 1999. A critical examination of the fundamental relations used in the analysis of nanoindentation data. J. Mater. Res. 14, 2296–2305.

Hill, R., Storåkers, B., Zdunek, A.B., 1989. A theoretical study of the Brinell hardness test. Proc. Roy. Soc. London A 423, 301–330.

Johnson, K.L., 1970. The correlation of indentation experiments. J. Mech. Phys. Solids 18, 115–126.

Johnson, K.L., 1985. Contact Mechanics. Cambridge University Press, Cambridge.

Joslin, D.L., Oliver, W.C., 1990. A new method for analyzing data from continuous depth-sensing microindentation tests. J. Mater. Res. 5, 123–134.

Knapp, J.A., Follstaedt, D.M., Myers, S.M., Barbour, J.C., Friedmann, T.A., 1999. Finite-element modeling of nanoindentation. J. Appl. Phys. 85, 1460–1474.

Larsson, P.L., 2001. Investigation of sharp contact at rigid-plastic conditions. Int. J. Mech. Sci. 43, 895–920.

Larsson, P.L., Giannakopoulos, A.E., Soderlund, E., Rowcliffe, D.J., Vesergaard, R., 1996. Analysis of Berkovich indentation. Int. J. Solids Struct. 33, 221–248.

Li, X., Bhushan, B., 2002. A review of nanoindentation continuous stiffness measurement technique and its applications. Mater. Character. 48, 11–36.

Lockett, F.J., 1963. Indentation of a rigid/plastic material by a conical indenter. J. Mech. Phys. Solids 11, 345–355.

Mata, M., Alcalá, J., 2003. Mechanical properties evaluation through indentation experiments in elasto-plastic and fully plastic contact regimes. J. Mater. Res. 18, 1705–11709.

Mata, M., Alcalá, J., 2004. The role of friction on sharp indentation. J. Mech. Phys. Solids 52, 145–165.

Mata, M., Anglada, M., Alcala, J., 2002. Contact deformation regimes around sharp indentations and the concept of the characteristic strain. J. Mater. Res. 17, 964–976.

Mendelson, A., 1968. Plasticity: Theory and Application. Macmillan, New York.

Mesarovic, S.D., Fleck, N.A., 1999. Spherical indentation of elastic–plastic solids. Proc. R. Soc. London A 455, 2707–2728.

Oliver, W.C., Pharr, G.M., 1992. An improved technique for determining hardness and elastic modulus using load and displacement sensing indentation experiments. J. Mater. Res. 7, 1564–1583.

Oliver, W.C., Pharr, G.M., 2004. Measurement of hardness and elastic modulus by instrumented indentation: advances in understanding and refinements to methodology. J. Mater. Res. 19, 3–20.

Tabor, D., 1951. Hardness of Metals. Clarendon Press, Oxford, UK.

Tabor, D., 1996. Indentation hardness: fifty years on—a personal view. Philos. Mag. A 74, 1207–1228.

Sakai, M., Akatsu, T., Numata, S., 2004. Finite element analysis for conical indentation unloading of elastic plastic materials with strain hardening. Acta Mater. 52, 2359–2364.

Sneddon, I.N., 1965. The relation between load and penetration in the axisymmetric Boussinesq problem for a punch of arbitrary profile. Int. J. Eng. Sci. 3, 47–57.

Suresh, S., Giannakopoulos, A.E., 1998. A new method for estimating residual stresses by instrumented sharp indentation. Acta Mater. 46, 5755–5762.

Storåkers, B., Biwa, S., Larsson, P.L., 1997. Similarity analysis of inelastic contact. Int. J. Solids Struct. 34, 3061–3083.

Tunvisut, K., O'Dowd, N.P., Busso, E.P., 2001. Use of scaling functions to determine mechanical properties of thin coatings from microindentation tests. Int. J. Solids Struct. 38, 335–351.

Umemoto, M., Liu, Z.G., Sugimoto, S., Tsuchiya, K., 2000. Tensile stress–strain analysis of single-structure steels. Metall. Mater. Trans. A 31A, 1785–1793.

Xu, Z.H., Rowcliffe, D., 2002. Method to determine the plastic properties of bulk materials by nanoindentation. Philos. Mag. A 82, 1893–1901.